Methylation index of Overly Branched tetraether lipids (MOB): a proxy for deep ocean (de)oxygenation?

Ronnakrit Rattanasriampaipong[1,2,3*] Yi Ge Zhang[1,4*], Olawale Alo[5], Xiao-Lei Liu[5], Yang Zhang[1,6], Bumsoo Kim[1,7], Franco Marcantonio[8], Franck Bassinot[9] and Tiegang Li[10]

[1]Department of Oceanography, Texas A&M University, College Station, TX, USA
[2]Department of Geosciences, The University of Arizona, Tucson, AZ, USA
[3]University Corporation for Atmospheric Research, Boulder, CO, USA
[4]State Key Laboratory for Isotope Geochemistry, Guangzhou Institute of Geochemistry, Chinese Academy of Sciences, Guangzhou, China
[5]School of Geosciences, The University of Oklahoma, Norman, OK, USA
[6]Frontiers Science Center for Deep Ocean Multispheres and Earth System, Key Lab of Submarine Geosciences and Prospecting Techniques, and College of Marine Geosciences, Ocean University of China, Qingdao, Shandong, China
[7]Department of Earth, Environmental and Planetary Sciences, Brown University, Providence, RI, USA
[8]Department of Geology & Geophysics, Texas A&M University, College Station, TX, USA
[9]Laboratoire des Sciences Du Climat et de L'Environnement, LSCE/IPSL, CEA-CNRS-UVSQ Université Paris-Saclay, Gif-sur-Yvette, Île-de-France, France
[10]Key Laboratory of Marine Sedimentology and Metallogeny, First Institute of Oceanography, Ministry of Natural Resources, Qingdao, China

*Corresponding author(s):
Ronnakrit Rattanasriampaipong (rrattan@ucar.edu) and Yi Ge Zhang (zhangyige@gig.ac.cn)
Postal address: 1040 E 4th St, Tucson, AZ 85721

Key Points

- We investigated surface and downcore marine sediments with a focus on overly and sparsely branched GDGTs.
- Degrees of methylation index of overly branched GDGTs strongly correlate to bottom water oxygen concentrations.
- The bottom ocean appears to be losing O_2 since the late Miocene, coupled with increasing export productivity and deep-water nutrient levels.

Abstract

Branched glycerol dialkyl glycerol tetraethers (brGDGTs) with lower (sparsely-branched; SB-) and higher (overly-branched; OB-) numbers of methylated branches relative to the "regular" brGDGTs (B-GDGTs) are abundant in anoxic waters in the Black Sea. Observed changes in abundances and numbers of methylated branches of the entire series OB-GDGTs, B-GDGTs, and SB-GDGTs relative to dissolved oxygen (DO) levels in anoxic waters suggest that these compounds can potentially track changes in oceanic DO levels through time. To explore this, we determine the entire brGDGT series in surface or near-surface sediments from sites with different DO distributions in marine waters and sediments, extending the limited core-top collection of these lipids. We propose a modified methylation index based on only OB-GDGTs, called MOB, to avoid the potential impacts of terrestrial-derived B-GDGTs. Interestingly, MOB values in our extended core-top collection are strongly related to changes in bottom-water DO concentrations rather than the site-specific minimum DO values, i.e. usually within mid-depth oxygen minimum zones (OMZs). This suggests that sedimentary lipids are likely derived from heterotrophic bacteria living at the sediment-water boundary in sediments while lipids produced within mid-depth OMZs are not effectively exported to deep oceans. Analysis of MOB values in ancient sediments in the East Equatorial Pacific shows a gradual decline in bottom water DO, correlating with the progressive increase in global export productivity, organic carbon burial, and elevated level of deep-water nutrient contents since the middle Miocene. These findings highlight the potential of MOB as a tool for reconstructing past oceanic (de)oxygenation events.

Keywords: bacterial tetraether lipids, dissolved oxygen, ocean (de)oxygenation, GDGTs, methylation index, MOB

Plain Language Summary

Membrane-spanning tetraether lipids of microbial organisms preserved in marine sediments, also known as "molecular fossils," have been widely used as geochemical proxies to infer environmental changes in the past. Overly branched and sparsely branched tetraether lipids are new classes of organic compounds that have recently been identified and found to be abundant in marine waters where oxygen levels are low. Despite its potential as an oxygen indicator in past oceans, only a few studies have determined these lipids in modern marine sediments. Here, we analyzed these lipids from surface marine sediments collected from various locations with different oxygen levels in the water and found a strong link between the presence of these branched lipids and the amount of dissolved oxygen in deep oceans. This suggests that microbes in surface marine sediments are likely the main source of these new types of lipids. With new information from this work, we propose a new proxy that can track changes in deep ocean oxygen concentrations Earth's history.

1 Introduction

Dissolved oxygen (DO) in the ocean is essential to all aerobic life. Instrumental records dating back to the 1960s confirm that DO concentrations in global oceans are declining in response to anthropogenic climate change (Cooley et al., 2022). The expansion of marine oxygen minimum zones (OMZ) in the tropics, such as in the Eastern Pacific Ocean, is one primary concern regarding oceanic changes in response to the ongoing deoxygenation (Busecke et al., 2022). Low DO levels in marine waters are harmful to marine life and can enhance the production of nitrous oxide, a potent greenhouse gas and a predominant ozone-depleting agent (Arévalo-Martínez et al., 2015; Ji et al., 2018). Moreover, the rise in numbers of hypoxic areas associated in human-induced factors, e.g. nutrient release, have been observed in lakes and coastal waters (Breitburg et al., 2018; Jenny et al., 2016). In global oceans, well-known marine regions with strong mid-depth OMZs are the Eastern Tropical Pacific Ocean, the Black Sea, and the Arabian Sea (**Boxes 2, 3,** and **4** in **Fig. 1A**). Because of the intrinsic interplay among various factors affecting marine OMZ regions, Earth system models have yet to provide a consistent projection of how these marine OMZs will change (cf. Busecke et al., 2022; Cabré et al., 2015). The reconstruction of past DO levels based on geochemical proxies offers an independent view that helps to understand marine OMZs in a warming world.

Quantifying levels of oxygen concentrations in paleo-oceans is typically complex and problematic due to the complexity of interplays across physical, chemical, and biological processes. Most geochemical proxies are linked to chemical cycling of nitrogen, sulfur, and carbon that are sensitive to redox conditions, from which past oxygen conditions are qualitatively inferred. Only a few geochemical and/or paleontological proxies have been quantitatively calibrated to DO levels in seawater. Examples of proxies that indirectly reflect changes in oxygen levels in seawater include but are not limited to, (i) concentrations of redox-sensitive trace metals, such as vanadium (V), uranium (U), molybdenum (Mo), and rhenium (Re), in sediments (Bennett and Canfield, 2020; Tribovillard et al., 2006), (ii) stable isotopic signatures of organic nitrogen ($\delta^{15}N$) bound in foraminiferal tests (cf. Auderset et al., 2019; Hess et al., 2023; Wang et al., 2022), and (iii) the ratio of trace elements incorporated to foraminiferal calcite to calcium, such as Mn/Ca (Barras et al., 2018) and I/Ca (Glock et al., 2014; Lu et al., 2020; Zhou et al., 2014). Porosity and pore density

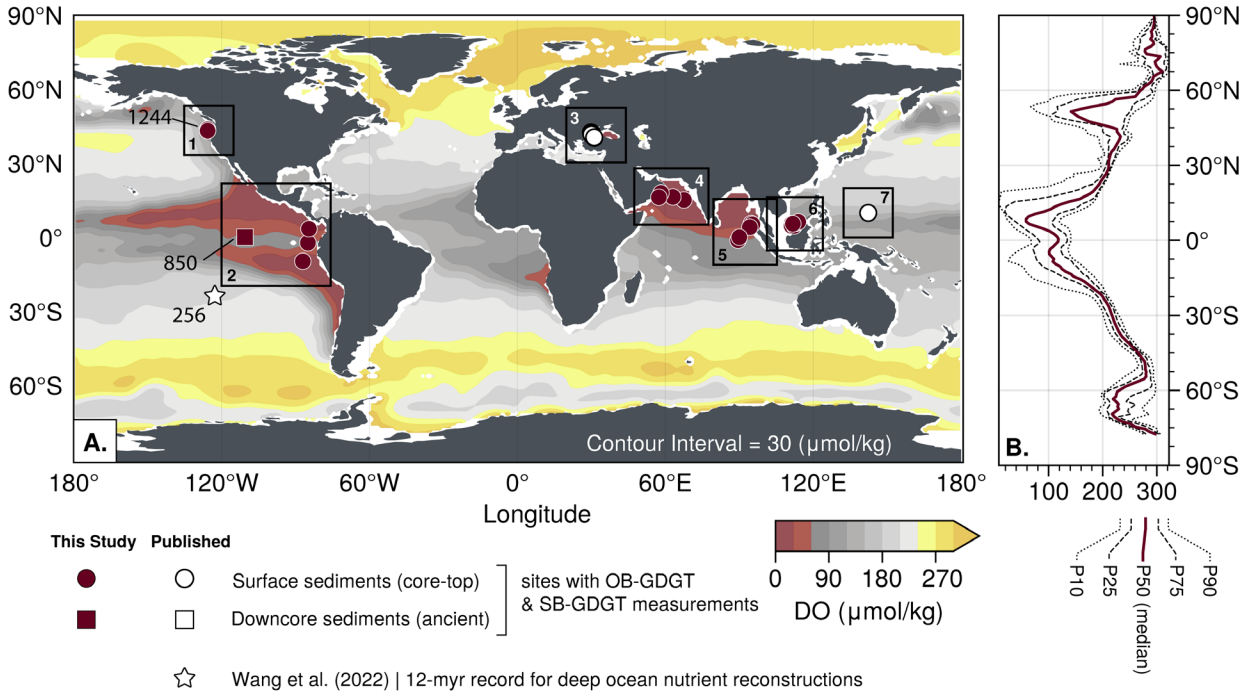

Fig. 1. Location of sites discussed in this study overlaid on the spatial distribution of dissolved oxygen concentrations at the 200-m depth level. (A) The map shows the modern locations of the study sites in our expanded data set. Tetraether lipids discussed in this paper were extracted and derived from surface sediments and down-core sediments. Sites with new GDGT measurements from this study are colored in maroon. Sites with published GDGT data are colored in white. The data set covers eight different marine regions, including (1) Pacific NW (Cascadia Margin), (2) Eastern Equatorial Pacific (EEP), (3) Western Tropical North Atlantic (WTNA) (Liu et al., 2014) (4) Black Sea (Liu et al., 2014), (5) Arabian Sea, (6) Eastern Equatorial Indian Ocean (EEIO), (7) South China Sea (SCS), and (8) Mariana Trench (Zeng et al., 2023). Shaded contours (Contour Interval "C.I." = 30) show the distribution of dissolved oxygen (DO) at 200-m water depth based on the 2018 World Ocean Atlas (WOA18) database (1°x1° spatial resolution). The shades of red indicate low oxygen conditions (<60 µmol/kg of seawater DO) (B) Latitudinal means of the 200-m WOA18 DO are also presented with P10, P25, P75, and P90 DO values.

of foraminifera is likely the only proxy that has evolved from a qualitative to a quantitative proxy (Glock et al., 2011; Rathburn et al., 2018). A quantitative organic proxy for DO levels in seawater has rarely been established.

Branched glycerol dialkyl glycerol tetraethers (brGDGT) are membrane-spanning lipids that were initially identified in samples from peatlands (Sinninghe Damsté et al., 2000) but later found to be ubiquitous in several environmental settings, including soils (e.g., Weijers et al., 2007), rivers (De Jonge et al., 2014; Zell et al., 2013), lakes (e.g., Buckles et al., 2014; Tierney and Russell, 2009), groundwaters (e.g., Ding et al., 2018), hydrothermal vents (e.g., Li et al., 2018), marine waters (e.g., Xie et al., 2014), and ocean sediments (e.g., Liu et al., 2012). The core

structures of brGDGT are ether-linked glycerol lipids with varying numbers of methylated branches and internal cyclopentane rings. The original determination of the chemical structures of "regular" brGDGT, hereafter B-GDGT, shows that the internal biphytanyl skeletons have 4–6 methyl branches and can contain up to two cyclopentyl moieties (Weijers et al., 2006b, 2007) (**Fig. 2**). Although the chemical structures of brGDGTs are similar to membrane-spanning isoprenoidal GDGT (isoGDGT) synthesized by marine Archaea, the stereochemical configuration of brGDGTs suggests bacterial sources (Weijers et al., 2006a).

Empirical observation of brGDGTs in natural archives shows that their compositional distributions are strongly correlated with environmental temperature and soil pH, which form the basis for several brGDGT-based environmental proxies (cf. Martínez-Sosa et al., 2021; Peterse et al., 2012; Raberg et al., 2023; Weijers et al., 2007). In marine settings, B-GDGT is generally low in abundance. Elevated concentrations of B-GDGT in marine sediments are typically assumed to be derived from terrestrial sources, as expressed by high values of the Branched versus Isoprenoid tetraether (BIT) index (Hopmans et al., 2004; Huguet et al., 2007). However, recent culture studies of a few known strains of *Acidobacteria* show that they synthesize brGDGTs in response to oxygen-limiting conditions (Chen et al., 2022; Halamka et al., 2023, 2021), suggesting that marine microbes that thrive in DO-stress environments may synthesize brGDGTs. As described by (Liu et al., 2012), two new brGDGT subclasses with relatively higher (overly branched; OB-) and lower (sparsely branched; SB-) numbers of methyl branches along glycerol backbones than the B-GDGT subclass (**Fig. 2**) have been found to be abundant in low DO marine waters from the Eastern Tropical North Pacific (Xie et al., 2014), the Black Sea, and the Cariaco Basin (Liu et al., 2014). They are also abundant in core-top sediments from the Black Sea (Liu et al., 2014). This collection of samples with the entire series of brGDGTs shows that concentrations of non-cycloalkylated brGDGTs and the degree of brGDGT methylation—as expressed by the Methylation Index of OB-GDGT, B-GDGT, and SB-GDGT ($MI_{OB/B/SB}$)—increase when DO levels decrease (Liu et al., 2014). Notably, the presence of OB-GDGT in ancient marine sediments deposited during Oceanic Anoxic Event 2 (OAE2; circa 94 Ma) suggests that these new subclasses of brGDGTs can be preserved in marine sediments for millions of years (Connock et al., 2022) and are likely related to low DO conditions in marine environments.

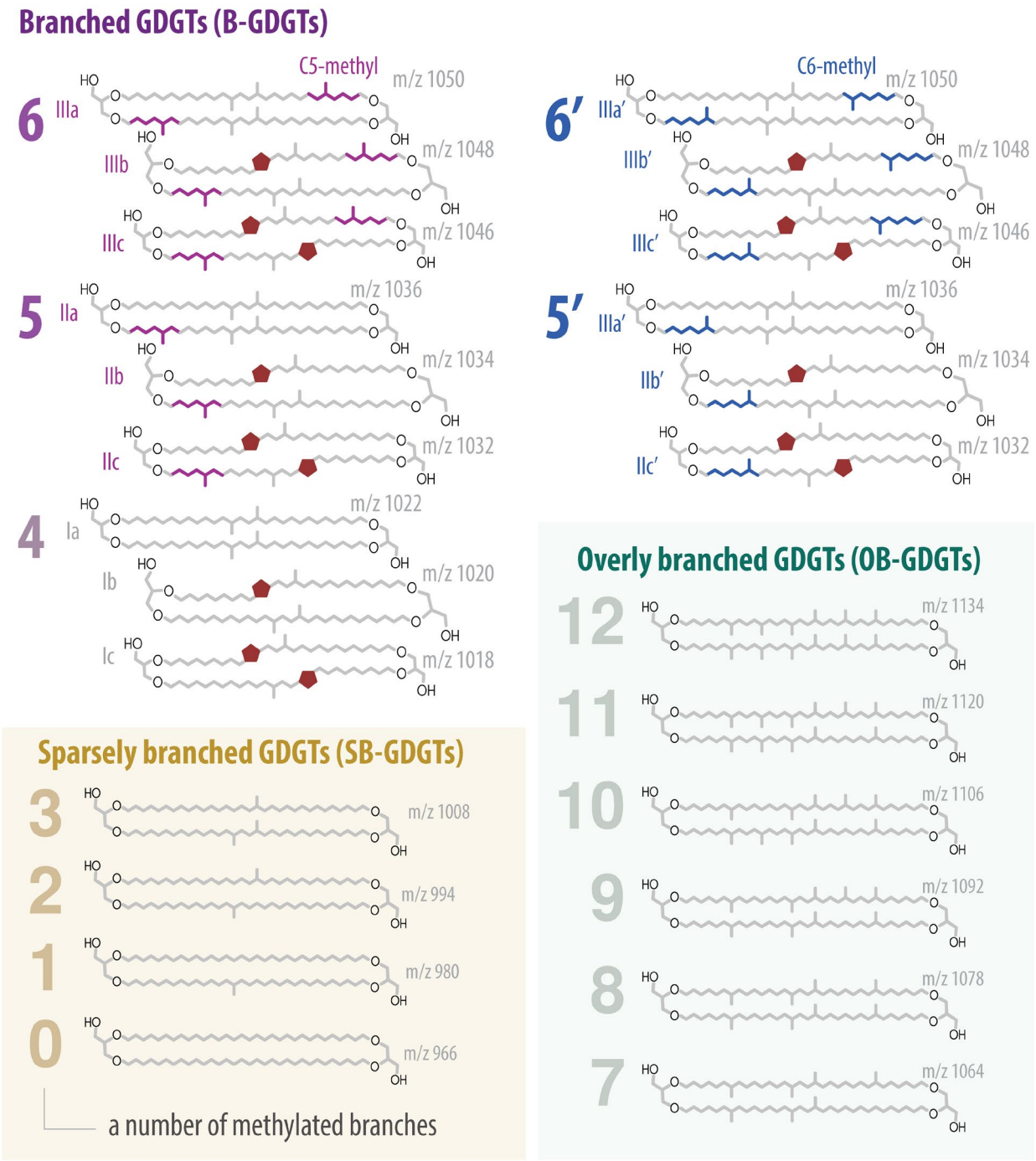

Fig. 2. Structures of tetraether lipids discussed in this study. Three main groups of non-isoprenoid branched glycerol dialkyl glycerol tetraethers (brGDGTs) discussed in this study are (1) regular branched GDGTs (B-GDGTs), (2) derivatives with fewer methylated branches, called sparsely-branched GDGTs (SB-GDGTs), and (3) derivatives with a higher number of methylated branches, called overly-branched GDGTs (OB-GDGTs). Mass-to-charge (m/z) ratios for each molecule are labeled on the upper right. The numbers labeled in front of each molecule represent a varying number of methylated branches. For B-GDGTs, structures for C5-methylated (left column) and C6-methylated (right column) B-GDGTs are shown separately.

136

Despite its great potential to be a proxy for marine (de)oxygenation, it is still unclear whether sedimentary OB-GDGT and SB-GDGT are mainly derived from mid-depth OMZs in open oceans. As recognized by Xie et al. (2014), suspended particulate matter (SPM) from depths below the OMZ in the Eastern Tropical North Pacific show low concentrations of the OB-GDGT and SB-GDGT fractions, indicating that (i) DO level in the OMZ is not low enough to trigger massive production of these lipids and/or (ii) there is no effective export mechanisms at intermediate water depths. Zeng et al. (2023) also recently investigated the distribution of brGDGT lipids in seafloor sediments from the Mariana Trench and have argued that relatively high abundances of OB-GDGT and SB-GDGT are synthesized by *unclassified* anaerobic bacterial communities in marine sediments unique to the hadal oceans. Although OB-GDGT and SB-GDGT in marine sediments were first described more than a decade ago (Liu et al., 2012), only a few studies reported these lipids in marine waters and sediments, making it difficult to evaluate the sources and their distributions in marine sediments fully.

Here, we report the distributions of the entire series of brGDGTs in surface marine sediments from five different regions, expanding the collection of existing published OB-GDGT and SB-GDGT data (**Fig. 1**). Alongside the down-core analysis, our aim is to identify the oxygen levels at which depths become the dominant controlling factor of the distribution of these brGDGTs. We further investigate the potential of the degree of methylation of OB-GDGTs as a quantitative organic geochemical proxy for past marine (de)oxygenation.

2 Materials and Methods

2.1 Data compilation and materials

Measurements of tetraether lipids with OB-GDGT and SB-GDGT fractions (n = 67) were compiled from four publications, and newly conducted by this study (see **Table 1**). This study determined fractional abundances of tetraether lipids extracted from the core-top (n = 24), near-surface (n = 4), and ancient marine sediments (n = 23). These data have expanded the spatial coverage of sites with OB-GDGT and SB-GDGT measurements spanning a wide range of vertical DO distributions in modern oceans (see **Figs. 1** and **3**). We grouped the based on their geographical distributions as follows: (1) Pacific Northwest, (2) Eastern Equatorial Pacific (EEP), (3) Black Sea, (4) Arabian Sea, (5) East Equatorial Indian Ocean (EEIO), (6) South China

Table 1. Information for study sites with GDGT measurements

	Region	Data Type	Cruise/Site	Source	Count
1	Pacific Northwest (Cascadian Ridge)	Near-surface	ODP 1244	This study	3
2	Eastern Equatorial Pacific (EEP)	Core top	MV1014_xx	This study	4
		Near-surface	ODP 850	This study	1
		Ancient	ODP 850	This study	23
3	Black Sea	Core top	BS_GeoB7xx	Liu et al. (2014)	12
4	Arabian Sea	Core top	MD77-2xx	This study	6
5	Eastern Equatorial Indian Ocean (EEIO)	Core top	BAR94-2x, MD77-159/160	This study	8
6	South China Sea (SCS)	Core top	WPxx	This study	6
7	Mariana Trench	Core top	MT03	Zeng et al. (2023)	4
				Total	**67**

Sea (SCS), and (7) Mariana Trench (see **Fig. 1**).

2.2.1 Surface and near surface marine sediments

For core-top GDGT samples, Eastern equatorial Pacific multi-corer samples were collected aboard the R/V *Melville* in 2010 (Marcantonio et al., 2014). Samples MV1014_01_01_MC (5°49.0863N, 85°44.528W; water depth 1760.4 m), MV1014_02_16_MC (00°10.8297'S, 85°52.0042'W; water depth 2846.0 m), and MV1014_03_20_MC (08°30.001'S, 87°02.695'W; water depth 4407.0 m) were collected from near the Cocos Ridge, Carnegie Ridge, and Peru Basin, respectively. The Cocos and Carnegie Ridge samples were collected from the margins of the Panama Basin, with the Carnegie Ridge multi-corer samples retrieved from a highly productive site (sediment mass accumulation rate, MARs) of about 4 $g \cdot cm^{-2} \cdot kyr^{-1}$, and the Cocos Ridge multi-corer samplers from a site that was not as productive and had a lower MAR (0.3 $g \cdot cm^{-2} \cdot kyr^{-1}$) (Marcantonio et al., 2014). The Peru Basin multi-corer samples were collected within the South Pacific oligotrophic gyre, and MARs could not be measured. The Arabian Sea piston cores MD77-200 (16°33.0'N, 67°54.0'E; water depth 2910 m), MD77-201 (17°33.6'N, 63°5.4'E; water depth 3665 m), MD77-204 (19°10.8'N, 58°15.6'E, water depth 1430 m), and MD77-205 (17°26.4'N, 57°24.0'E; water depth 969 m) were collected aboard the R/V *Marion Dufresne* in 1977 from the

Arabian Sea during the OSIRIS 3 campaign (Jean-Claude, 1977). For EEIO, core-top samples were from two different expeditions. The first set of samples MD77-159 (0°4.2'N; water depth 4241 m) and MD77-160 (1°15.0'N, 90°1.8'E; water depth 2160 m) were collected during the same cruise OSIRIS 3. The second set of samples BAR94-24 (6°44.4'N, 94°50.46'E; water depth 2676 m), BAR94-25 (6°26.1'N, 95°19.5'E; water depth 1558 m), and BAR94-27 (5°20.4'N, 94°18.3'E; water depth 2689 m) were collected aboard R/V *Baruna Jaya I* during the 1994 BARAT campaign (Guichard and Hardjawidjaksana, 1994). For SCS, core-top samples WP01 (6°40.458'N, 111°13.92'E; water depth 1848 m), WP02 (5°51.522'N, 111°14.094'E; water depth 1289 m), WP03 (5°52.146'N, 112°18.072'E; water depth 687 m), WP04 (6°55.704'N, 113°6.744'E; water depth 1569 m), WP05 (7°28.446'N, 113°54.852'E; water depth 913 m), and WP06 (6°41.01'N, 111°45.534'E; water depth 1926 m) were collected aboard the R/V *Ke Xue Yi Hao* (formerly named *Kexue I*) during the South China Sea Survey Cruise in 2012.

We also investigate shallow down-core GDGT data with sampling depth shallower than 10 meters, including samples from the Mariana Trench (Zeng et al., 2023), the EEP ODP Site 850, and the Cascadia Margin and treat them as shallow "core-top" samples to maximize the number of observations for the core-top data set and its spatial coverage. Given persistent low O_2 conditions in the Cascadian Ridge region since 32,000 years ago (cf. Saravanan et al., 2020), GDGT distributions of ODP Site 1244C down-core sediments dated ~30,000 years old are not expected to be very different from surface sediments (44°35.1702'N, 125°7.1902'W; modern water depth 895.1 m below sea level (mbsl); sampling depths ~7–8 m deep; see **Fig. 1**).

2.2.2 Lipid extracts derived from ancient marine sediments

For paleo-GDGT samples, we determined GDGT distributions from 24 polar lipid fractions derived from ancient sediments from the Ocean Drilling Program (ODP) Site 850 (1°17.838'N, 110°31.284'W; modern water depth 3786.1 m; see **Fig. 1**). The samples selected for this study are a subset of the original data set used to reconstruct the SST history of EEP over the past 12 million years (Zhang et al., 2014).

2.2 Lipid analysis

2.2.1 Sample preparation

Total lipid extracts (TLEs) derived from surface, near-surface, and down-core marine sediments were prepared at Texas A&M University. Forty-one marine sediment samples (~0.5–13 g) were freeze-dried and homogenized with mortar and pestle. The grounded sediments were then subjected to lipid extraction using a Dionex 350 Accelerated Solvent Extractor (ASE) with 9:1 (v/v) dichloromethane/methanol at 120°C and 10.34 MPa for five static cycles. Subsequently, the TLEs were dried in an ultrapure nitrogen stream and stored in 2 ml vials for subsequent analysis.

2.2.2 GDGT determination

GDGT determinations were performed at the University of Oklahoma. Sample preparation and analytical setup are modified after Connock et al. (2022). Each TLE sample was redissolved in 1 ml pure MeOH, ultrasonicated for 10 minutes, and centrifuged at 3000 rpm for five minutes. Following centrifugation, 500 µl of the TLE redissolved in MeOH were transferred into a 2 ml injection vial for lipid analysis. Reversed-phase high-performance liquid chromatography coupled to electrospray ionization quadrupole time-of-flight mass spectrometry (RP-HPLC-ESI-Q-TOF-MS) was performed with an Agilent 1290 series UPLC system coupled to an Agilent 6530 Q-TOF mass spectrometer through an Agilent jet stream dual electrospray ionization (AJS-ESI) interface. For each TLE sample, 10 µl out of the 500 µl volume were injected onto an ACE UltraCore Super C18 column (5 µm, 2.1 × 250 mm, ACE, Aberdeen, UK) maintained at 45 °C. Following method parameters were set to achieve the separation of GDGTs: (i) For Q-TOF, voltages of 3500 V, 175 V, 65 V, 750 V were set for a capillary, a fragmentor, a skimmer, an octupole, respectively, in auto MS/MS scanning mode with MS range of m/z 50-2000 and MS/MS range of m/z 20-2000. (ii) For ESI, the drying gas (N_2) temperature was set at 300 °C with the flow rate of 8 L min^{-1} and the nebulizer gas (N_2) pressure of 35 PSIG. For RP-HPLC, two eluents, A and B, were used. Eluent A was 95:5:0.04:0.10 of methanol/H_2O/formic acid/14.8 M NH_3 (aq.), and eluent B was 50:50:0.04:0.10 of hexane/2-propanol/formic acid/14.8 M NH_3 (aq.). A flow rate of 0.2 mL min^{-1}, first hold 100% A for 5 min, and to 70% A and 30% B in 25 min, followed by a gradient to 50% B at 50 min and hold for 5 min, and finally re-equilibrated with 100% eluent A at a flow rate of 0.4 mL min^{-1} for 5 min. GDGTs were identified based on accurate masses, retention time, and diagnostic fragments. Quantification was achieved with an extraction window of $[M+H]^+$ being ± 0.02 m/z units. We quantified relative abundances for four main subclasses of GDGT in all new

GDGT measurements, including isoGDGTs, B-GDGTs, OB-GDGTs, and SB-GDGTs, without separating C5- and C6-methyl derivatives.

2.3 Dissolved Oxygen in Seawater for Modern GDGT Data

2.3.1 Site-specific DO vertical profiles

Sampling sites of surface sediments with new GDGT measurements from this study have expanded from previously published works, representing a more comprehensive range of different DO distributions in water columns (see **Fig. 3**). We use objectively analyzed climatological mean fields of the DO data set (named *o_an*; 1°x1° spatial resolution; 0–5500 meters at standard depth levels; 1900–2017) from the 2018 World Ocean Atlas (WOA18) database (Garcia et al., 2019) to determine different degrees of (de)oxygenation in the water column above each sampling site. We read the WOA18 DO data set (*NetCDF file*) using the *Xarray* Python library (Hoyer and Hamman, 2017) to perform all the data manipulation and matching. The sampling coordinates (latitude, longitude) of the GDGT data were matched to the closest grid using the built-in *nearest* method. We limited the deepest depth of any matched WOA18 DO profiles using the sampling depth of the GDGT data. For the Mariana Trench core top data, we used the in situ measurements of DO collected during the descent of the cable of a conductivity-temperature-depth (CTD) device at the Challenger Deep of the Mariana Trench (11°22.569'N, 142°18.105'E; deepest sampling depth 10000 m) in December 2015 (Tian et al., 2018) as the WOA18 DO data is unavailable for the entire water column. The location of the CTD cast at Challenger Deep is approximately 29 kilometers from the MT3 core site (cf. Zeng et al., 2023), reasonably comparable to the 1°x1° spatial resolution of the WOA18 DO data set.

2.3.2 DO-derived parameters reflecting different degrees of oxygenation in seawater

To determine the position in the water column where the strongest response of brGDGT distributions to different degrees of oxygenation occur, we calculated parameters that reflect degrees of oxygenation at different locations and depth ranges in each DO vertical profile. **Fig. 4** shows an example DO vertical profile with annotated positions and depth ranges of DO-derived parameters, including ① ***minOxy***, ② ***insituOxy***, ③ ***oxycline2oxymin***, ④ ***normIntgOMZ***, ⑤ ***surface2insitu***, ⑥ ***oxycline2insitu***, and ⑦ ***OMZdepthRatio***. Three key depth levels needed for

the calculation of these parameters are (i) the *oxycline* depth, (ii) the *bottomOMZ* depth, and (iii) the sampling depth (in situ depth). The fastest rate of declining DO concentrations from surface defines the *oxycline* depth. The *bottomOMZ* depth is defined by the fastest rate of increase in the DO concentration below the *oxycline* depth.

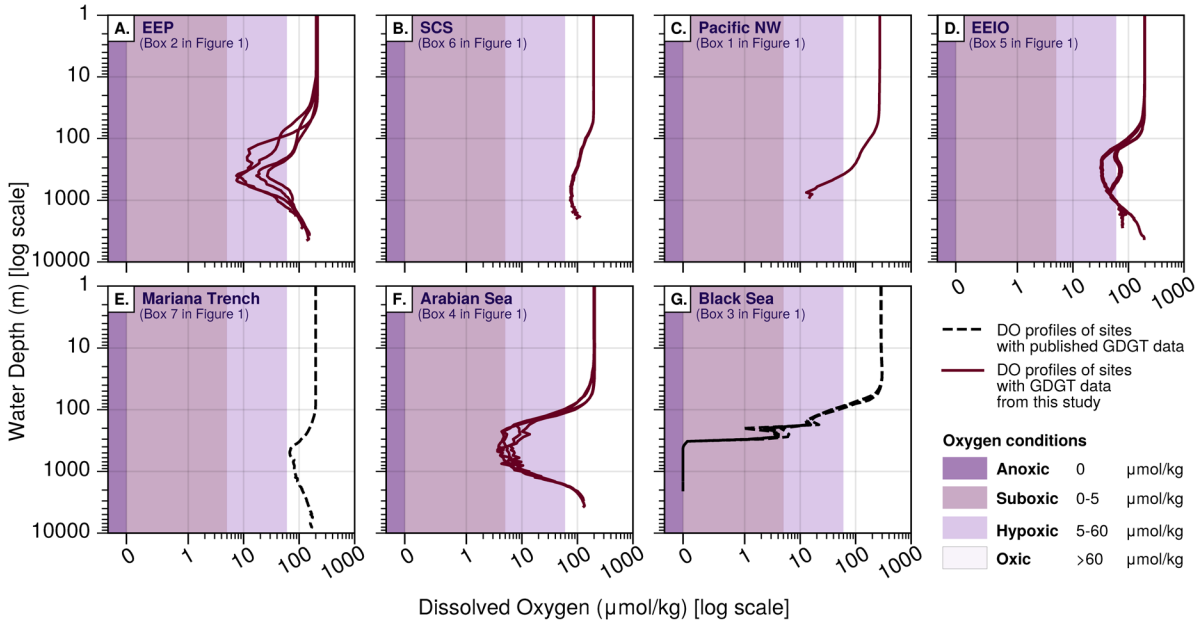

Fig. 3. Overview of the vertical distributions of dissolved oxygen (DO) concentrations. Each subplot shows the vertical DO distributions above surface sediment sampling sites at different regions shown in Fig. 1: (A) Eastern Equatorial Pacific (EEP), (B) South China Sea (SCS), (C) Pacific Northwest (Pacific NW), (D) Eastern Equatorial Indian Ocean (EEIO), (E) Mariana Trench, (F) Arabian Sea, and (G) Black Sea. Black dashed lines are DO profiles of sites with published GDGT data. Maroon solid lines are DO profiles of sites with GDGT data from this study. Shades of purples indicate different oxygen conditions: anoxic (0 µmol/kg; dark purple), suboxic (0–5 µmol/kg; purple), hypoxic (5–60 µmol/kg; pale purple), and oxic (>60 µmol/kg; white).

3 Results and Discussion

3.1 Degree of methylation of brGDGTs at different oxygen conditions

The Methylation Index of OB-GDGT, B-GDGT, and SB-GDGT ($MI_{OB/B/SB}$) has been proposed by Liu et al. (2014) to track the changes in both fractional abundances and degrees of methylation for the entire series of brGDGTs. To avoid confusion of the $MI_{OB/B/SB}$ index with the Methane Index (abbreviated as MI; Zhang et al., 2011), we propose the new abbreviation as "DMI" (Degree of Methylation of brGDGTs Index). This new DMI abbreviation also differs from the fractional abundance ratio of B-GDGTs with different methylated branches, i.e., the Methylation of Branched Tetraethers (abbreviated as MBT; Weijers et al., 2007). The higher values of

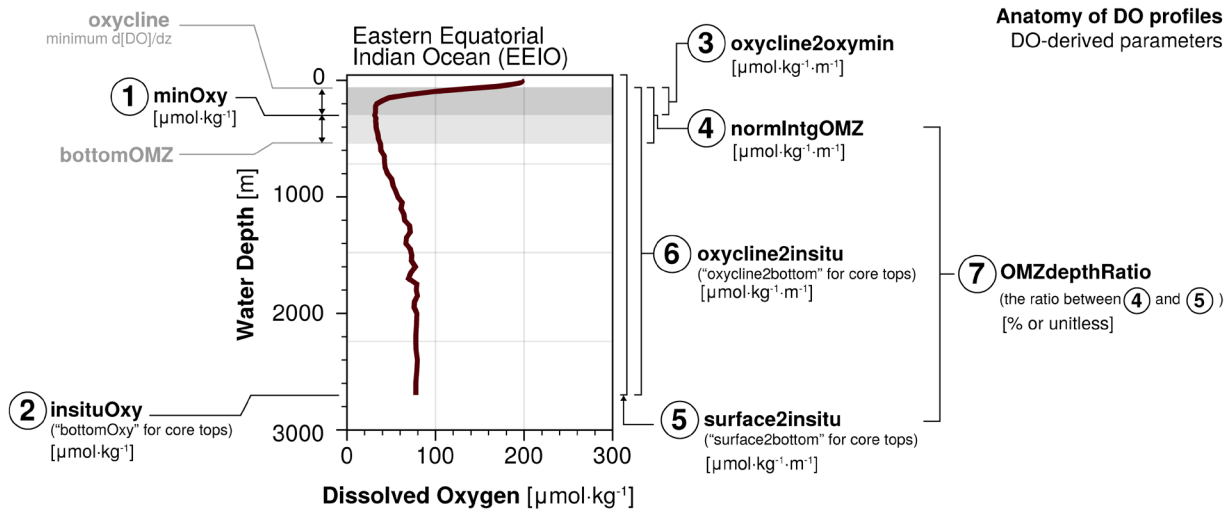

Fig. 4. An example DO profile with annotations of DO-related parameters. Seven different DO-related parameters were calculated from a site-specific DO vertical profile using the 2018 World Ocean Atlas database (Garcia et al., 2019).

281 $DMI_{OB/B/SB}$ reflect the distributional shift towards brGDGT structures with higher numbers of
282 methylated branches. The equation of $MI_{OB/B/SB}$ is expressed as follows:

$$DMI_{OB/B/SB} = \frac{(\sum_{n=7}^{12} n * [X_{OB}]) + (\sum_{n=4}^{6} n * [X_B]) + (\sum_{n=0}^{3} n * [X_{SB}])}{[\Sigma OB + \Sigma B + \Sigma SB]} \quad (1)$$

283 where $[X_{OB}]$, $[X_B]$, and $[X_{SB}]$ represent fractional abundances for OB-GDGT, B-GDGT, and SB-
284 GDGT, respectively, while *n* denotes the number of methylated branches of each GDGT fraction.
285 If sedimentary OB-GDGT and SB-GDGT are derived primarily from the mid-depth OMZ in the
286 water column, the value ranges of $MI_{OB/B/SB}$ of samples from places where strong OMZs exhibit
287 in the water column (*minOxy* < 60 µmol·kg^{-1} DO) should be higher and *significantly different* from
288 places where mid-depth water are oxic (*minOxy* ≥ 60 µmol·kg^{-1} DO). Given the small sample size
289 and non-Gaussian distribution in each data set, we chose the non-parametric Mann-Whitney U test
290 (MWU; also called the Wilcoxon rank-sum test) to assess whether the medians between oxic and
291 low oxygen data clusters differ *significantly*. The resulting *p* value (p<.01) suggests that the
292 medians of the two clusters are *significantly different* from each other; however, the value ranges
293 between low oxygen and oxic clusters overlap in large part (**Fig. 5A**). It should be noted that new
294 GDGT measurements from this study emphasize the distinction in the $DMI_{OB/B/SB}$ value ranges
295 between low oxygen and oxic conditions compared to the clusters of the limited collection of
296 published data (maroon versus gray dots in **Fig. 5A**).

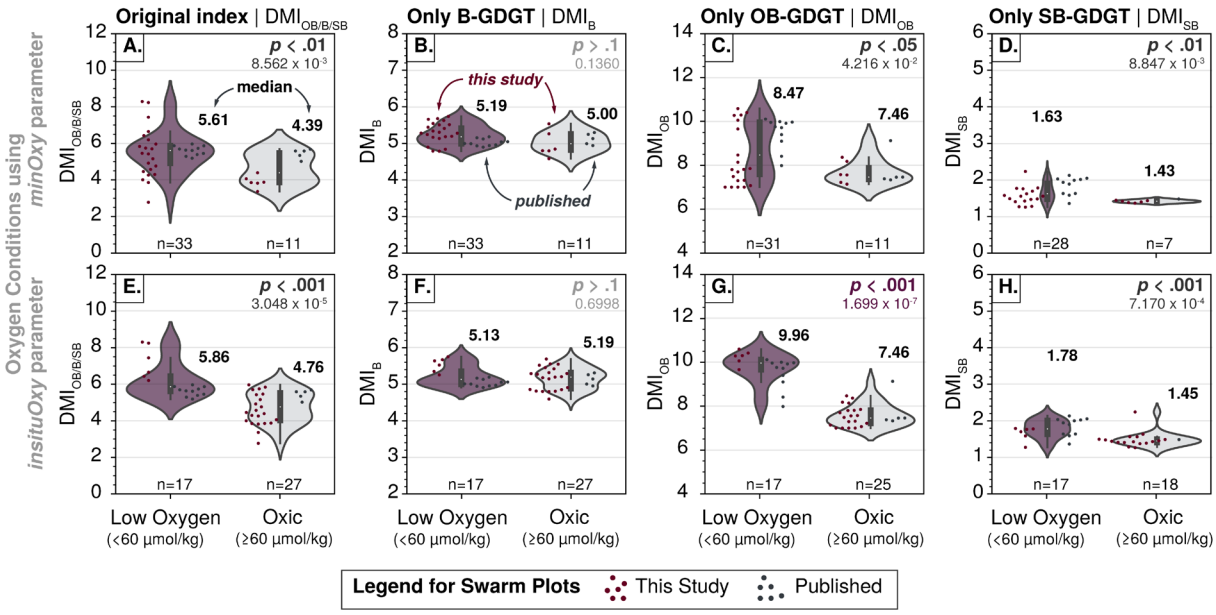

Fig. 5. Ranges of methylation indices of core-top GDGT data at low oxygen and oxic conditions based on *minOxy* and *insituOxy* parameters. GDGT data were classified into low oxygen (purple violins) and oxic (gray violins) conditions based on *minOxy* (top row) and *insituOxy* (BWO for core-top data; bottom row). Each column shows value ranges of different methylation indices discussed in this study, including the original methylation index $MI_{OB/B/SB}$ (left) and three modified methylation indices based on only B-GDGT (middle left), OB-GDGT (middle right), and SB-GDGT (right) fractions. Violin plots show the distribution of methylation indices as a symmetric kernel density estimate (KDE) together with the inner box-and-whisker plot. White dots show the medians of each data cluster with the numerical annotations presented next to each violin plot. Swarm plots (dots) show the distribution of raw data points from this study (maroon) and published data (dark gray). Note: The annotated *p* values are from the non-parametric Mann-Whitney *U* test. Grey out annotated text indicates that the medians are *not significantly different* between low oxygen and oxic data clusters (*p>.1*). Purple annotated text indicates the case with lowest *p* value across all comparisons. Actual *p* values up to fourth significance digit are shown below the reported significance level.

As B-GDGT fractions are known to have multiple sources, notably non-marine, we assess if removing B-GDGT from the calculation will improve the separation between low oxygen and oxic data clusters. The modified indices are expressed as follows:

$$\mathrm{DMI_{OB/B}} = \frac{(\sum_{n=7}^{12} \mathrm{n} * [\mathrm{X}_{OB}] + \sum_{n=4}^{6} \mathrm{n} * [\mathrm{X}_{B}])}{[\Sigma OB + \Sigma B]} \quad (2)$$

$$\mathrm{DMI_{B/SB}} = \frac{(\sum_{n=4}^{6} \mathrm{n} * [\mathrm{X}_{B}] + \sum_{n=0}^{3} \mathrm{n} * [\mathrm{X}_{SB}])}{[\Sigma O + \Sigma SB]} \quad (3)$$

$$\mathrm{DMI_{B}} = \frac{(\sum_{n=4}^{6} \mathrm{n} * [\mathrm{X}_{B}])}{[\Sigma B]} \quad (4)$$

$$\mathrm{DMI_{SB}} = \frac{(\sum_{n=0}^{3} \mathrm{n} * [\mathrm{X}_{SB}])}{[\Sigma SB]} \quad (5)$$

$$\mathrm{DMI_{OB}} = \frac{(\sum_{n=7}^{12} \mathrm{n} * [\mathrm{X}_{OB}])}{[\Sigma OB]} \quad (6)$$

The MWU test for these modified methylation indices shows that the medians of the methylation index based only on the B-GDGT series (DMI_B) between the low oxygen and oxic data clusters are *not significantly different* (p>.1; **Fig. 5B**). While the resulting p values for the methylation indices based only OB-GDGT (DMI_{OB}) and SB-GDGT (DMI_{SB}) series are below the standard significance level (p <.05; **Figs. 5C** and **5D**), suggesting that distributions of OB-GDGT and SB-GDGT are sensitive to *minOxy* and *insituOxy* levels. The greater difference in the medians between the low oxygen and oxic data clusters in the $DMI_{OB,}$ i.e., the lower resulting p value, suggests that OB-GDGTs may be more sensitive to changes in oxygen conditions in the water column.

Although the discovery of OB-GDGT and SB-GDGT series and the establishment of the $DMI_{OB/B/SB}$ index were originally from studies that focus on regions with strong mid-depth OMZs or fully anoxic water columns (Liu et al., 2012, 2014; Xie et al., 2014), we expanded our assessment on the variation of methylation indices in response to changes in oxygen conditions at different locations in the water column using the calculated DO-derived parameters. Based on the nonparametric Spearman's rank correlation, the $DMI_{OB/B/SB}$ show the overall negative correlation with oxygen conditions in the water column; higher $DMI_{OB/B/SB}$ at lower oxygen conditions (Column 5 in **Fig. 6**). Across all seven DO-derived parameters, the *minOxy* parameter gives the highest Spearman's rank correlation coefficient (denoted as *rho* or ρ) of -0.58 with the $DMI_{OB/B/SB}$ (Column 5 & Row 1 in **Fig. 6**). As suggested above by the MWU tests, the DMI_{OB} should show better responses to changes in oxygen conditions in the water column. However, correlation coefficients between *minOxy* and DMI_{OB} and DMI_{SB} indices exhibit similar (ρ = -0.59) or stronger responses (ρ = -0.66), respectively. Interestingly, the *insituOxy* gives a stronger Spearman's ρ with the DMI_{OB} (-0.78) than the *minOxy* parameter (C10 in **Fig. 6**). In fact, the Spearman's correlation between the *insituOxy* parameter and the DMI_{OB} shows the strongest correlation across the heatmap of the pairwise correlation (C10 & R2 in **Fig. 6**), hinting to us that changes in surface sediment OB-GDGT distributions might be largely controlled by oxygen conditions at the deep ocean instead of the intermediate depth. By repeating the MWU tests for the *insituOxy* case, we observe stronger differences in the medians between low oxygen and oxic data clusters, i.e., lower

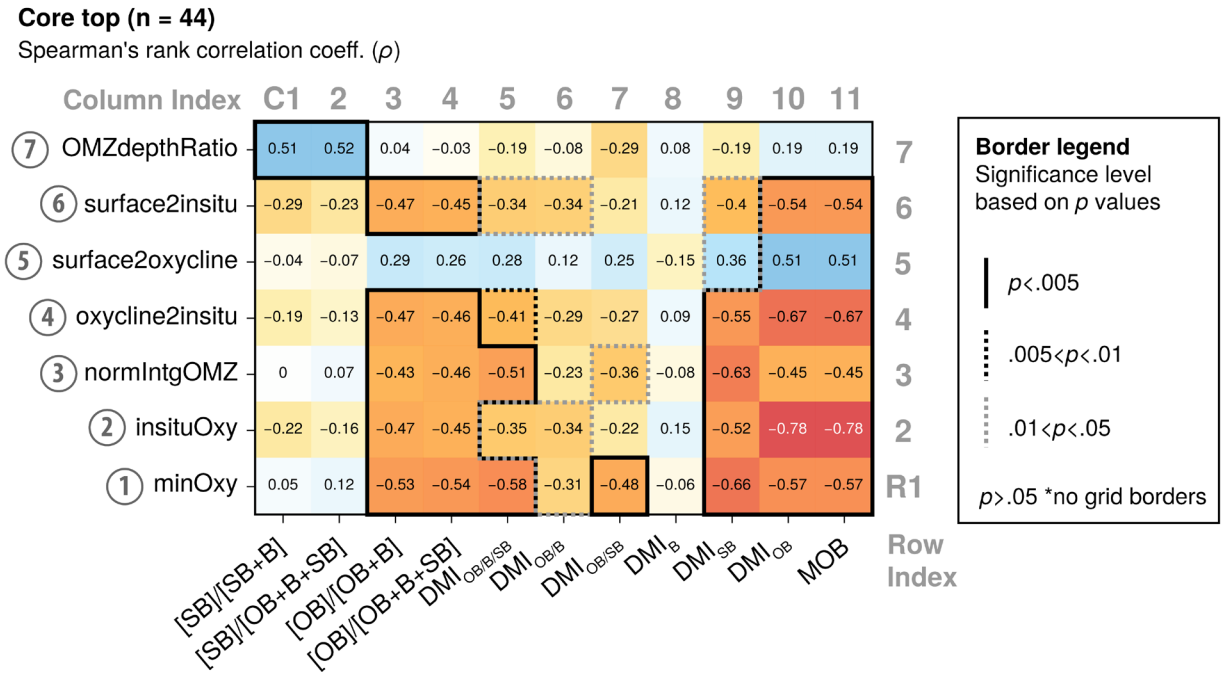

Fig. 6. Pairwise correlation between brGDGT-derived indices and DO-derived parameters. The heatmap shows Spearman's rank correlation coefficient (ρ) between DO-derived parameters (rows) and GDGT-derived indices (columns) with the annotated numerical values rounded to the second decimal place. The "HotCold" color map emphasizes the direction of the trend between the two variables. The annotated grid borders indicate significance level based on p values: $p<.005$ (solid black), $.005<p<.01$ (dashed black), $.01<p<.05$ (dashed gray), and $p>.05$ (no border; *not statistically significance*).The position where each DO-derived parameter represent in the water column can be found in **Fig. 4**.

328 p values, in all methylation indices except the DMI_B (see the bottom row in **Fig. 5**). The largest
329 difference in the medians and the lowest p value observed from the DMI_{OB} case (**Fig. 5G**), together
330 with the strongest Spearman's correlation (C10 & R2 in **Fig. 6**), all indicate that the OB-GDGTs
331 might be the GDGT fraction that is most sensitive to changes in oxygen conditions in the water
332 column. Across all analyses, it appears that changes in deep ocean oxygen conditions, i.e.,
333 specifically at the seawater-sediment interface in our study, exert stronger control over the
334 distribution of OB-GDGT and SB-GDGT in surface marine sediments than oxygen conditions of
335 the overlying water column.

336 ### 3.2 Potential sources of OB-GDGT and SB-GDGT in marine sediments

337 Our statistical analyses over the extended data set of core-top brGDGTs suggest that the
338 likely sources of these lipids are heterotrophic bacteria thriving in the sediment-water interface,
339 rather than the mid-depth OMZs. This is in line with the observation from the water-column SPM
340 study in the EEP, showing that OB-GDGT and SB-GDGT are rapidly disappearing in the

oxygenated water masses below the mid-depth OMZs (Xie et al., 2014). However, the production of OB-GDGT in marine sediments below the seafloor could alter the original distribution of brGDGT in the surface sediments, challenging the idea of using these lipids as a geochemical proxy to reconstruct past changes in ocean oxygenation. Research by Zeng et al. (2023) suggests that OB-GDGTs are produced by anaerobic bacteria in subsurface sediments collected from the Mariana Trench, supported by the co-occurrence of a high abundance of bacterial 16S rRNA genes and an increase in the relative abundance of known anaerobic bacteria unique to abyssal marine sediments. Unfortunately, paired porewater chemistry profile critical for understanding the sediment column's redox condition of in the context of microbial ecology and lipid distribution changes were unavailable (Zeng et al., 2023). Additionally, studies on intact polar lipids, which are more closely related to living cells, suggest that they typically constitute a very small portion of GDGT found in the sediment column (typically <15%; cf. Lengger et al., 2014; Lipp and Hinrichs, 2009; Liu et al., 2011). Most sedimentary GDGTs fall into the core lipid fraction, representing the inactive pool long after cell lysis. Future work such as lipid analysis of bacterial cultures, is needed to confirm the extent to which these subsurface bacteria contribute to the sedimentary pool of OB-GDGTs. Intact polar lipids of OB-GDGTs can also help quantify the contribution of living bacteria to the total GDGT pool.

Another piece of evidence unfavorable for subsurface production as the primary source of these lipids comes from our analysis of brGDGT distributions from ancient marine sediments of ODP site 850, dated back 12 million years. If OB-GDGTs with higher degrees of methylation were primarily produced in subsurface anoxic sediments, we would expect higher DMI_{OB} values from the intervals where porewater chemistry clearly indicates redox condition changes (Shipboard Scientific Party, 1992). The presumed low oxygen conditions in downcore sediments start at approximately 110 meters below sea floor, where concentrations of porewater ammonia and methane gas increase with decreasing sulfate (**Figs. 7D–F**). The DMI_{OB} values within this presumed anoxic interval show a relatively low DMI_{OB} index, arguing against major *in situ* GDGT production by anaerobic bacteria in sediments. With the help of the global core-top data, we are able to infer bottom water oxygen levels through the temporal variation in the DMI_{OB} index. Mechanistically, these changes can be recorded by alterations in bacterial communities at the seawater-sediment interface or by physiological responses of cell membranes to different in situ oxygen levels by the same group of bacteria.

3.3 Development of a proxy for deep ocean (de)oxygenation

3.3.1 The Methylation index of Overly Branched GDGTs (MOB)

Although OB-GDGT and SB-GDGT series are present in most of core-top sediments in the extended data set, SB-GDGTs are generally of very low abundance in downcore samples and were often not reported in previous work (cf. Connock et al., 2022; Zeng et al., 2023). Due to their low abundance, we did not report SB-GDGT fractions from our reanalyzed samples from ODP 850 (see **Fig. 7A**). Given that OB-GDGT fractions are observed in both modern and ancient marine sediment archives, the DMI_{OB} index emerges as the most suitable index to be developed as a proxy for tracking (de)oxygenation in past oceans. We normalized the DMI_{OB} index to the entire data set

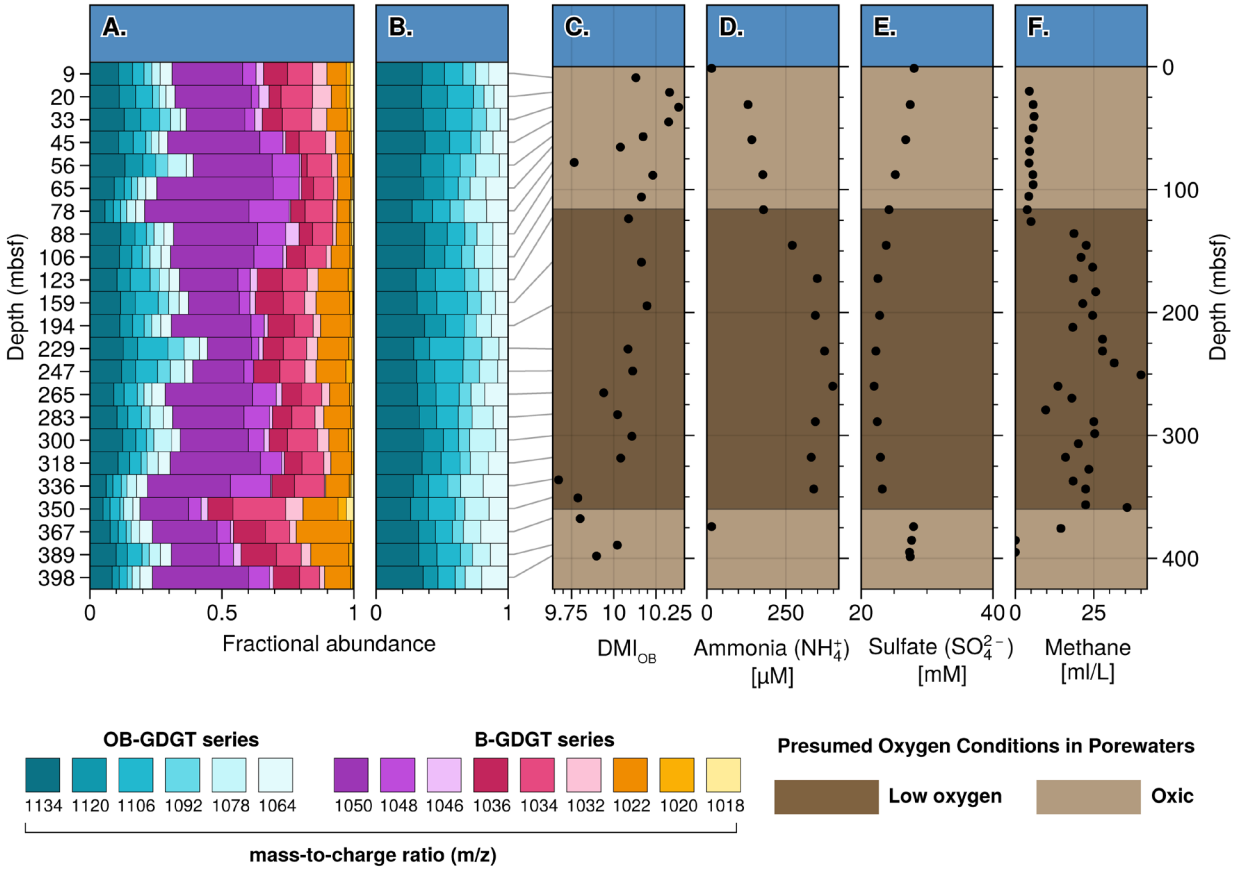

Fig. 7. Downcore brGDGT distribution, DMI_{OB}, and porewater chemistry of sediments from Ocean Drilling Program site 850. (A) Fractional abundances of OB-GDGT and B-GDGT series. (B) Fractional abundances of OB-GDGT series. (C) The modified methylation index uses only the OB-GDGT series (MI_{OB}). The stored TLEs were analyzed samples used in Zhang et al. (2014) temperature reconstruction study. Concentrations of (D) porewater ammonia (NH_4^+), (E) porewater sulfate (SO_4^{2-}), and (F) methane gases in sediments collected during the ODP850 expedition (Shipboard Scientific Party, 1992). The dark brown layer indicates the presumed low oxygen conditions in sediments based on porewater chemistry. Note: Fractional abundances of brGDGTs were measured from the stored TLEs extracted from downcore sediments from the Ocean Drilling Program (ODP) site 850.

using the minimum-maximum scaling technique to scale the index value range to span from 0 to 1 and named the **M**ethylation index of **O**verly **B**ranched GDGT as the **MOB** index:

$$MOB = \frac{(\mathrm{DMI}_{OB})_{observed} - (\mathrm{DMI}_{OB})_{min}}{(\mathrm{DMI}_{OB})_{max} - (\mathrm{DMI}_{OB})_{min}} \quad (7)$$

where $(\mathrm{DMI_{OB}})_{observed}$ is the methylation index of OB-GDGT derived from **equation (6)**. The theoretical minimum $(\mathrm{DMI_{OB}})_{min}$ and maximum $(\mathrm{DMI_{OB}})_{max}$ values of the $\mathrm{DMI_{OB}}$ index are 7 and 12, respectively. Plugging these values into **equation (7)**, the MOB values can be calculated as follows:

$$MOB = \frac{(\mathrm{DMI}_{OB})_{observed} - 7}{12 - 7} = \frac{(\mathrm{DMI}_{OB})_{observed} - 7}{5} \quad (8)$$

The MOB index gives the same Spearman's correlation ρ as the $\mathrm{DMI_{OB}}$ with the strongest negative relationship against the *insituOxy* parameter (C11 & R2 in **Fig. 6**).

3.3.2 Bottom water oxygen calibrations based on the extended core-top data set.

Given the relatively small sample size (n = 42) of the core-top data set, it is likely that the distributions of the MOB index and *insituOxy* are non-Gaussian. Plus, the value ranges of both parameters are strictly positive, including zeros $[0,\infty)$, suggesting that the ordinary least square (OLS) might not be the most suitable choice of regression model as it assumes that the MOB and *insituOxy* can go to negative values. Utilizing the *Tweedie Regressor* from the *scikit-learn* Python library, we found that the Poisson-like regression (power = 1.0) provides the highest deviance score (D^2 = 0.66; p = 0.06; see **Figs. 8A** and **8C**). The Poisson-like regression is the Generalized Linear Model (GLM) with the natural log link function and can be expressed in the following form:

$$Y = e^{\alpha + \beta \cdot X} + \epsilon \quad (9)$$

where the target Y value is the exponential of a linear model with intercept (α), slope (β), and random noise (ϵ). The quality of each Poisson-like regression is quantified by the percentage of deviance explained (D^2) of the GLM; the score that is equivalent to the coefficient of determination

402 r^2 in the OLS regression.

403 Although we have expanded the core-top collection with samples from sites represented a
404 wider range of oxygen conditions in water column, the regression curves could still be heavily
405 biased towards this anoxic/euxinic basin as data from the Black Sea (n = 12) represented ~29% of
406 the entire core-top collection (n = 42). We repeated the same set of regressions on the subset of
407 core top data excluding the Black Sea data to provide alternative calibrations that may be more
408 suitable for open-ocean settings. Similarly, the Poisson-like regression also gives the highest
409 deviance score the *insituOxy* and MOB parameters (D^2 = 0.67; p = 0.09; see **Figs. 8B** and **8D**).
410 However, the y-intercept of the latter case is higher than the regression curve of the full core-top
411 dataset. To fully capture the possible range of estimated Y values at any given X, we computed the
412 95% confidence interval of the Poisson-like regression curves by randomly sampling α and β

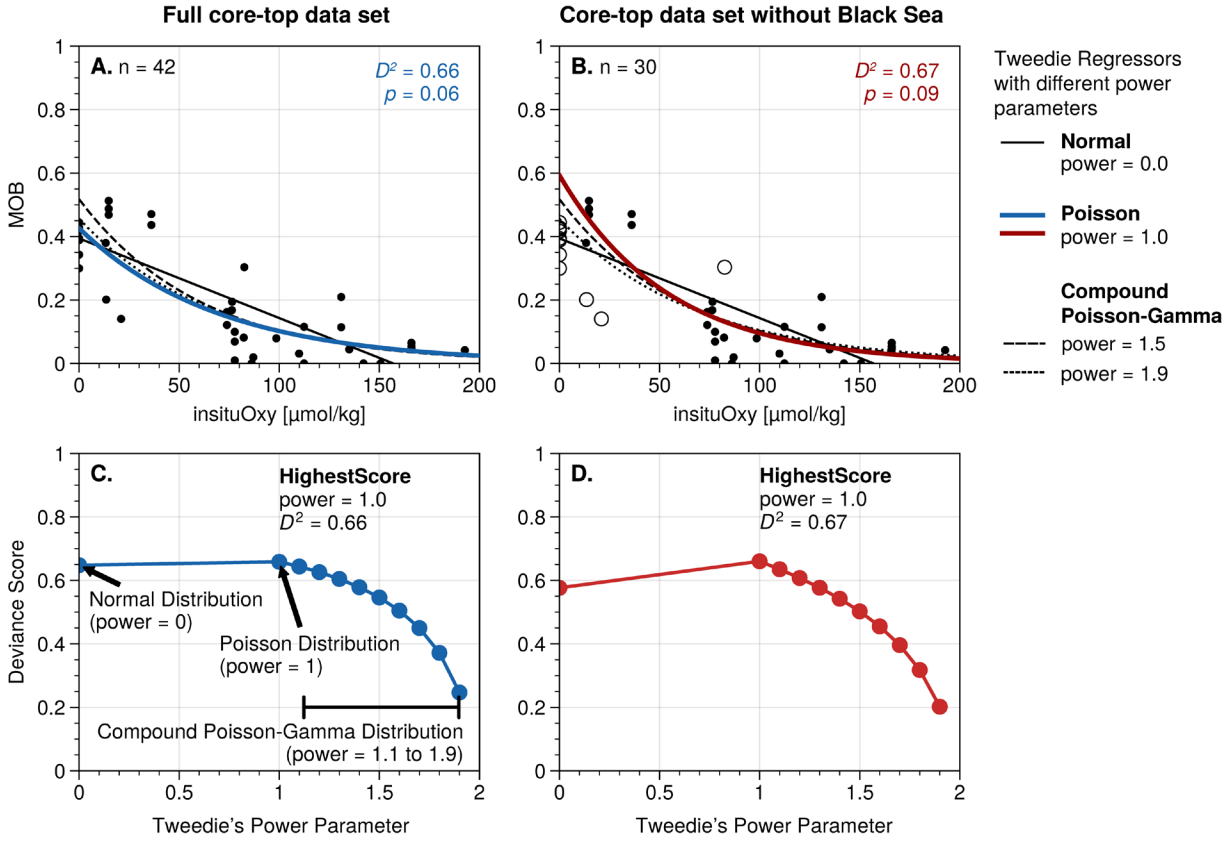

Fig. 8. Different calibration curves based on the extended core-top GDGT data set. Several choices of calibration curves are displayed over MOB-insituOxy scatter plots based on (A) the full core-top and (B) the core-top data set without the Black Sea samples. Calibration curves result from generalized linear models (GLM) with different Tweedie's power parameters. At different power parameters, GLM predicts the MOB values (fitted MOB) by assuming that fitted Y values belong to a distribution in the exponential dispersion model (EDM), including the Normal (power = 0.0), the Poisson (power = 1.0), and the Compound Poisson-Gamma (power = 1.1-1.9) distributions. (Bottom) Deviance scores for each GLM regression result at different Tweedie's power parameters for (C) the full core-top data set and (D) the subset of GDGT collection without the Black Sea.

parameters using the Markov Chain Monte Carlo (MCMC) technique (**Figs. 9A** and **9B**). Although the deviance score is only slightly improved without Black Sea data in the core-top data set, the Poisson-like regression based on this subset is preferred for the *insituOxy*-MOB core-top calibration as the resulting MOB residuals show no relationship with the fitted MOB values (**Fig. 9G**). The fitted MOB values based on the full data set show a stronger regression bias, i.e. higher r^2 in the residual plot (**Fig. 9F**). **Table 2** shows slopes and intercepts of both regression scenarios.

3.4 Application of MOB: EEP deoxygenation over the past 12 million years

As previously discussed, we view that the down-core variation in the MOB index as likely reflecting bacterial community at the seawater-sediment interface in response to different levels of

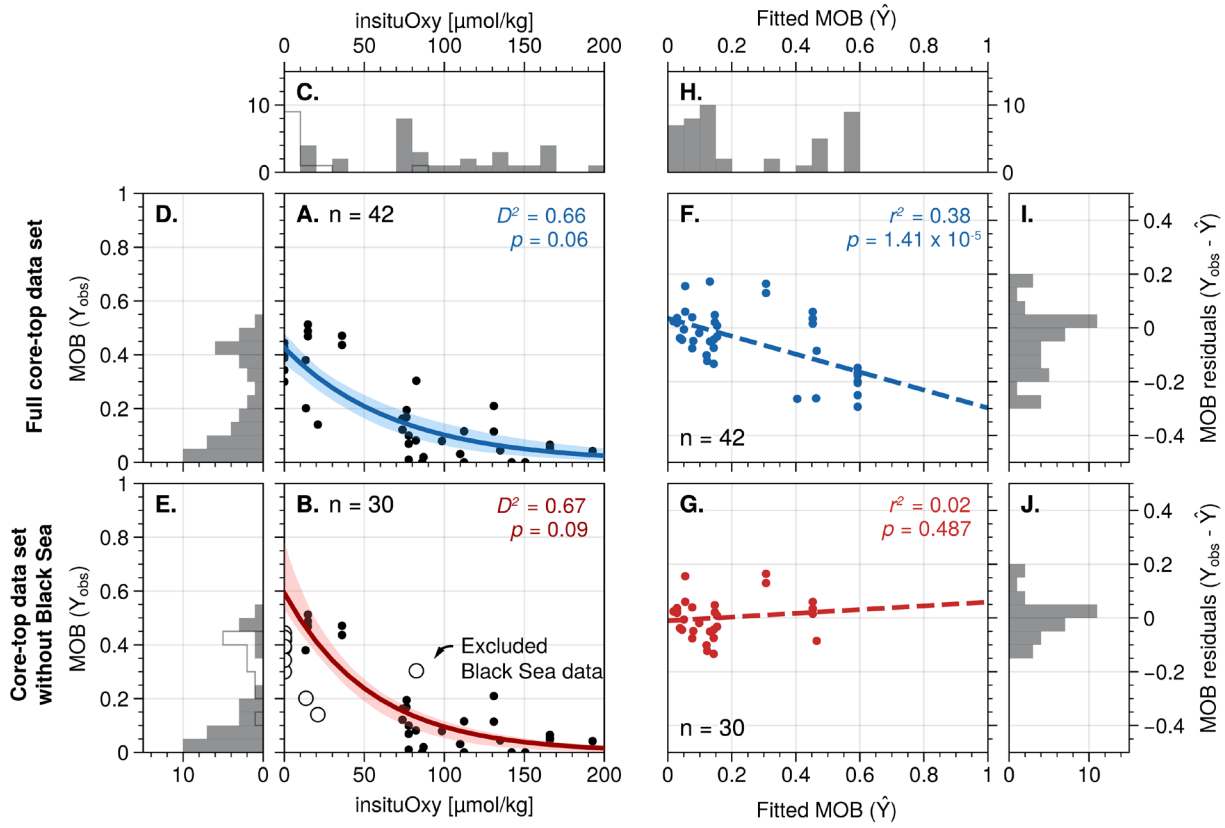

Fig. 9. Poisson-like regressions between *insituOxy* and MOB index with residual plots based on the full core-top data set (top) and the subset without Black Sea data (bottom). (A) The Poisson-like regression curve of the full core-top data set with the annotated deviance score (D^2) and the *p value*. The shaded area represents the 95% confidence interval of the Poisson-like regression line using the Markov Chain Monte Carlo technique to capture the full range of regression slopes and intercepts. (B) The scatter plot of the residuals between the observed and fitted MOB values (observed MOB - fitted MOB) with associated r^2 and *p* values. (F) and (G) are the same regression analysis as (A) and (B) but for the subset of core-top collection with the Black Sea data. (C-E and H-J) Histograms show data distributions of *X* and *Y* variables of each scatter plot.

Table 2. Slopes and intercepts for Poisson-like regression curves discussed in main text.

Case No.	Equation	Intercept (α)	Slope (β)	D^2	*p* value	Ref. Fig.
	Poisson-like regression $MOB = exp(\alpha + \beta \cdot insituOxy) + \varepsilon$ **Equation (9)**					
(1)	Full core-top data set	-0.8535	-0.01431	0.66	0.06	Fig. 8A
(2)	Core-top data set without Black Sea	-0.5223	-0.01827	0.67	0.09	Fig. 8B

bottom water O_2 concentrations, referred to as *insituOxy* parameter in this study, over geologic history. Using the Poisson-like regression parameters for the open ocean case (without Black Sea data; **Regression Case 2** in **Table 2**), the estimated *insituOxy* concentrations based on the MOB index show that the bottom water masses at ODP Site 850 underwent low DO conditions for the entire 12-myr record. Reconstructed *insituOxy* estimates gradually decreased from approximately 20 $\mu mol \cdot kg^{-1}$ during the late Miocene to approximately 10 $\mu mol \cdot kg^{-1}$ during the Plio-Pliestocene epochs with two spikes of increasing *insituOxy* observed around 10 and 4 million years ago (**Fig. 10A**). Although there are no equivalent independent proxy records to confirm the reconstructed *insituOxy* concentrations based on the MOB index, some indirect evidence suggests that deep water in EEP experienced low O_2 conditions during cooling episodes. For example, several reconstructions of bottom water O_2 levels based on redox-sensitive authigenic uranium derived from marine sediments spanning the last 180,000 years show the lowest values during glacial periods, suggesting an increased extent of respired carbon in the deep ocean (cf. Marcantonio et al., 2020). In addition, estimated changes in bottom water O_2 concentrations based on the output of a geochemical box model CYCLOPS in the deep Pacific during the Last Glacial Maximum relative to the Holocene can be up to approximately 80–100 $\mu mol \cdot kg^{-1}$ (see a thorough discussion in Studer et al., 2021), reflecting low O_2 concentrations in the deep Pacific.

Variation in oxygen supply to deep ocean waters could also be attributed to changes in climate and ocean circulation. The cooling climate during the Neogene (Herbert et al., 2016; Zachos et al., 2001), the development of modern-like Antactic Circumpolar Current since the late Miocene (Evangelinos et al., 2024), and the intensification of Pacific Deep Water ciculation since the early Pliocene (Yin et al., 2022) all could have caused an increase in deep-water DO concentrations due to (i) greater gas solubility in colder seawaters and (ii) stronger export of oxygen-rich deep water masses from high-latitude formation sites. Yet, our interpreted low DO

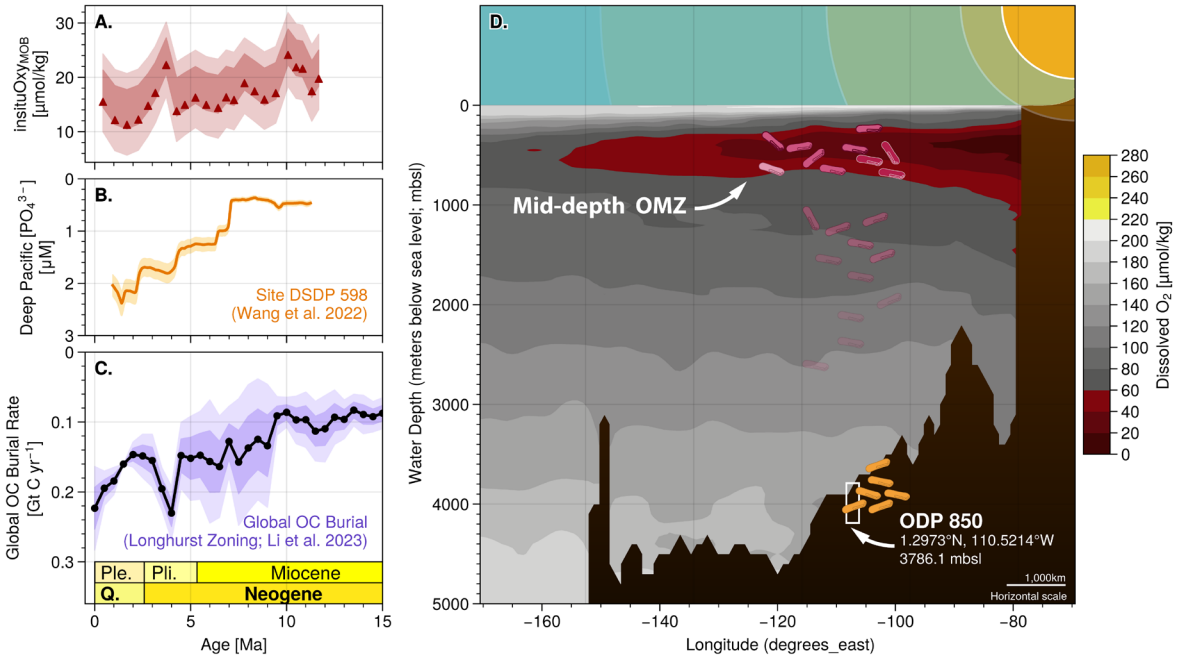

Fig. 10. 12-myr records of the MOB index in the Eastern Pacific Ocean. (A) Reconstructed *insituOxy* based on Poisson-like (log-linear) calibration. Red triangles represent the estimated *insituOxy* based on regression parameters resulting from the data set without the Black Sea data (Case 2 in Table 2). Shaded bands show the corresponding confidence intervals of 68% (±1σ) and 95% (±2σ), estimated using an MCMC approach. (B) Deep Pacific phosphate concentrations [PO_4^{3-}] reconstructed from the nearby ocean drilling site DSDP 598 in the EEP region. Increases in deep-water [PO_4^{3-}] over the past 12 myr reflect the declining level of deep ocean DO, as previously discussed by Wang et al., (2022). (D) Global organic carbon burial rate estimated from global (D) Graphical sketch shows the proposed mechanism how oxygen conditions in deep Pacific changes over time at ODP site 850.

conditions in the deep EEP based on the MOB index parallels with the observed increase in deep Pacific water phosphate levels (see **Figs. 9B** and **9C**; Wang et al., 2022) and the overall increase in global organic carbon burial rate over the last 15 Ma (Li et al., 2023), suggesting to us that enhanced oxygen supply was outcompeted by higher oxygen demand attributed to increased export productivity. It remains unclear whether declining oxygen levels drive enhanced export productivity and nutrient enrichment, or if they are merely a response to increased organic matter export and subsequent degradation. Nonetheless, the secular trend of increasing bottom water nutrient levels, declining oxygen concentrations, and enhanced organic carbon burial in sediments presents a coherent narrative of ocean biogeochemical changes since the middle Miocene in the EEP region, carrying important implications for long-term climatic and oceanic changes.

Despite incorporating the shallowest sample from ODP Site 850 into the core-top collection, it is still possible that the absolute values of reconstructed *insituOxy* concentrations based on our current calibration are still be biased towards lower DO levels given the limited extent

of represented sites in the current data set. However, this first iteration of MOB proxy development shows that the variation in methylation index of OB-GDGT can track the overall declining trend of deep ocean DO concentrations. Future studies with additional GDGT measurements from a wider range of core-top sites can be easily incorporated into the calibration framework using the Python codes (see Supplementary Information) and would improve the accuracy of the absolute *insituOxy* estimates based on the MOB index.

3.5 Potential avenues for future works

Similar to other well-established GDGT-based proxies like MBT/CBT and TEX_{86}, which have provided major insights into Earth's past environments despite initially limited information on the source organisms, the MOB proxy could offer unique insights into past oceanic redox conditions, with profound implications for understanding the co-evolution of life and global biogeochemical cycles. While our interpretation relies on certain assumptions, the empirical relationship between MOB values and bottom water oxygen levels observed in the core-top study is a promising beginning. Future work is needed to validate and refine this proxy; for example, identifying source organisms of these lipid compounds. Furthermore, confirming the resistance of OB-GDGTs to early diagenesis or understanding any potential preferential degradation patterns would strengthen the robustness of this proxy.

4 Conclusions

Since its first discovery from core-top sediments in the EEP region (Liu et al., 2012), OB-GDGTs have demonstrated great potential to be a geochemical proxy for past marine (de)oxygenation. Building upon the original methylation index of brGDGTs ($DMI_{OB/B/SB}$), we explored relationships between various combinations of brGDGT ratios/indices and environmental variables related to DO in ocean water columns. We found that the modified methylation index using only OB-GDGT (DMI_{OB}) in the core top data set gives the strongest response to *insituOxy* concentrations. Applying the proposed MOB index to the paleo GDGT record spanning the last 12 myr from the EEP region suggests to us that the index can track progressive deoxygenation in the deep Pacific parallel to the elevated nutrient level of the Pacific deep water (Wang et al., 2022) and enhanced burial of organic carbon globally (Li et al., 2023). Regression analyses performed in this work can easily accommodate new core-top data, when available, to improve the accuracy

of the prediction model for bottom water oxygen concentrations. Our findings demonstrate the MOB index's potential for tracking relative changes in deep-ocean (de)oxygenation through time, highlighting its promising application as a proxy for past oceanic redox conditions intrinsically linked to global biogeochemical cycles and climate history.

Data Availability Statement.

GDGT data. Published GDGT fractional abundance data used for in the study are directly retrieved from Liu et al. (2014) and Zeng et al. (2023). The curated data sets of these data together with new GDGT data determined by this study are available as supplementary materials in this article and are deposited online at Figshare (public link will be provided upon acceptance) and GitHub repositories (to be provided at the proofing stage, if accepted).

Python codes. Jupyter Notebooks (**.ipynb*) containing Python codes that were used for data preparation, statistical analyses, and data visualization are also deposited at Figshare repositories (to be provided at the proofing stage, if accepted) and available at github.com/PaleoLipidRR/brGDGT-oxy-proxy/ (to be published at the proofing stage, if accepted) or upon request from the corresponding author

CRediT authorship contribution statement.

Ronnakrit Rattanasriampaipong: Writing – original draft, Writing – review & editing, Visualization, Formal analysis, Conceptualization, Investigation, Data Curation, Methodology.
Yi Ge Zhang: Conceptualization, Writing – review & editing, Methodology, Coordination and oversees the project.
Olawale Alo: Methodology – GDGT determination, Writing – review & editing,
Xiao-Lei Liu: Methodology – GDGT determination, Writing – review & editing,
Yang Zhang: Methodology – GDGT determination
Bumsoo Kim: Methodology – Sample preparation, Writing – review & editing
Franco Marcantonio: Writing – review & editing, Resources – obtain sediment materials
Franck Bassinot: Resources – obtain sediment materials
Tiegang Li: Resources – obtain sediment materials

Acknowledgement.

We thank the captains and scientific/operational crews of all research cruises from which samples used in this study were obtained, including R/V *Melville* (2010 campaign), R/V *Marion Dufresne* (OSIRIS 3 campaign), R/V *Baruna Jaya I* (BARAT campaign), and R/V *Ke Xue Yi Hao* (2012

campaign). We thank Ethan Grossman, Jason Sylvan, and Robert Korty for their thoughtful comments and discussion. Partial financial support for this study was provided by the Texas A&M University Dissertation Fellowship and NOAA Climate & Global Change Postdoctoral Fellowship administered by UCAR's Cooperative Programs for the Advancement of Earth System Science (CPAESS) under the NOAA Science Collaboration Program award (NA21OAR4310383) to R.R., Guangzhou Institute of Geochemistry and Chinese Academy of Sciences Start-up support for Y.G.Z, Texas Sea Grant Grants-In-Aid of Graduate Research Program (NA18OAR4170088) to B.K.

Declaration of competing interest. The authors declare that they have no known competing financial interests or personal relationships that could have appeared to influence the work reported in this paper.

References

Arévalo-Martínez, D.L., Kock, A., Löscher, C.R., Schmitz, R.A., Bange, H.W., 2015. Massive nitrous oxide emissions from the tropical South Pacific Ocean. Nat. Geosci. 8, 530–533. https://doi.org/10.1038/ngeo2469

Auderset, A., Martínez-García, A., Tiedemann, R., Hasenfratz, A.P., Eglinton, T.I., Schiebel, R., Sigman, D.M., Haug, G.H., 2019. Gulf Stream intensification after the early Pliocene shoaling of the Central American Seaway. Earth Planet. Sci. Lett. 520, 268–278. https://doi.org/10.1016/j.epsl.2019.05.022

Barras, C., Mouret, A., Nardelli, M.P., Metzger, E., Petersen, J., La, C., Filipsson, H.L., Jorissen, F., 2018. Experimental calibration of manganese incorporation in foraminiferal calcite. Geochim. Cosmochim. Acta 237, 49–64. https://doi.org/10.1016/j.gca.2018.06.009

Bennett, W.W., Canfield, D.E., 2020. Redox-sensitive trace metals as paleoredox proxies: A review and analysis of data from modern sediments. Earth-Sci. Rev. 204, 103175. https://doi.org/10.1016/j.earscirev.2020.103175

Breitburg, D., Levin, L.A., Oschlies, A., Grégoire, M., Chavez, F.P., Conley, D.J., Garçon, V., Gilbert, D., Gutiérrez, D., Isensee, K., Jacinto, G.S., Limburg, K.E., Montes, I., Naqvi, S.W.A., Pitcher, G.C., Rabalais, N.N., Roman, M.R., Rose, K.A., Seibel, B.A., Telszewski, M., Yasuhara, M., Zhang, J., 2018. Declining oxygen in the global ocean and coastal waters. Science 359, eaam7240. https://doi.org/10.1126/science.aam7240

Buckles, L.K., Weijers, J.W.H., Verschuren, D., Sinninghe Damsté, J.S., 2014. Sources of core and intact branched tetraether membrane lipids in the lacustrine environment: Anatomy of Lake Challa and its catchment, equatorial East Africa. Geochim. Cosmochim. Acta 140, 106–126. https://doi.org/10.1016/j.gca.2014.04.042

Busecke, J.J.M., Resplandy, L., Ditkovsky, S.J., John, J.G., 2022. Diverging Fates of the Pacific Ocean Oxygen Minimum Zone and Its Core in a Warming World. AGU Advances 3, e2021AV000470. https://doi.org/10.1029/2021AV000470

Cabré, A., Marinov, I., Bernardello, R., Bianchi, D., 2015. Oxygen minimum zones in the tropical Pacific across CMIP5 models: mean state differences and climate change trends. Biogeosciences 12, 5429–5454. https://doi.org/10.5194/bg-12-5429-2015

Chen, Y., Zheng, F., Yang, H., Yang, W., Wu, R., Liu, X., Liang, H., Chen, H., Pei, H., Zhang, C., Pancost, R.D., Zeng, Z., 2022. The production of diverse brGDGTs by an Acidobacterium providing a physiological basis for paleoclimate proxies. Geochim. Cosmochim. Acta 337, 155–165. https://doi.org/10.1016/j.gca.2022.08.033

Connock, G.T., Owens, J.D., Liu, X.-L., 2022. Biotic induction and microbial ecological dynamics of Oceanic Anoxic Event 2. Communications Earth & Environment 3, 136. https://doi.org/10.1038/s43247-022-00466-x

Cooley, S., Schoeman, D., Bopp, L., Boyd, P., Donner, S., Ito, S.-I., Kiessling, W., Martinetto, P., Ojea, E., Racault, M.-F., 2022. Oceans and coastal ecosystems and their services, in: IPCC AR6 WGII. Cambridge University Press.

De Jonge, C., Stadnitskaia, A., Hopmans, E.C., Cherkashov, G., Fedotov, A., Sinninghe Damsté, J.S., 2014. In situ produced branched glycerol dialkyl glycerol tetraethers in suspended particulate matter from the Yenisei River, Eastern Siberia. Geochim. Cosmochim. Acta 125, 476–491. https://doi.org/10.1016/j.gca.2013.10.031

Ding, S., Kohlhepp, B., Trumbore, S., Küsel, K., Totsche, K.-U., Pohnert, G., Gleixner, G., Schwab, V.F., 2018. In situ production of core and intact bacterial and archaeal tetraether lipids in groundwater. Org. Geochem. 126, 1–12.

https://doi.org/10.1016/j.orggeochem.2018.10.005
Evangelinos, D., Etourneau, J., van de Flierdt, T., Crosta, X., Jeandel, C., Flores, J.-A., Harwood, D.M., Valero, L., Ducassou, E., Sauermilch, I., Klocker, A., Cacho, I., Pena, L.D., Kreissig, K., Benoit, M., Belhadj, M., Paredes, E., Garcia-Solsona, E., López-Quirós, A., Salabarnada, A., Escutia, C., 2024. Late Miocene onset of the modern Antarctic Circumpolar Current. Nat. Geosci. 17, 165–170. https://doi.org/10.1038/s41561-023-01356-3
Garcia, H.E., Weathers, K.W., Paver, C.R., Smolyar, I., Boyer, T.P., Locarnini, M.M., Zweng, M.M., Mishonov, A.V., Baranova, O.K., Seidov, D., 2019. World Ocean Atlas 2018, Volume 3: Dissolved Oxygen, Apparent Oxygen Utilization, and Dissolved Oxygen Saturation.
Glock, N., Eisenhauer, A., Milker, Y., Liebetrau, V., Schönfeld, J., Mallon, J., Sommer, S., Hensen, C., 2011. ENVIRONMENTAL INFLUENCES ON THE PORE DENSITY OF BOLIVINA SPISSA (CUSHMAN). J. Foraminiferal Res. 41, 22–32. https://doi.org/10.2113/gsjfr.41.1.22
Glock, N., Liebetrau, V., Eisenhauer, A., 2014. I/Ca ratios in benthic foraminifera from the Peruvian oxygen minimum zone: analytical methodology and evaluation as proxy for redox conditions. Biogeosci. Discuss. 11, 11635–11670. https://doi.org/10.5194/bgd-11-11635-2014
Guichard, F., Hardjawidjaksana, K., 1994. BARAT 94 cruise, R/V \emphBaruna Jaya I.
Halamka, T.A., McFarlin, J.M., Younkin, A.D., Depoy, J., Dildar, N., Kopf, S.H., 2021. Oxygen limitation can trigger the production of branched GDGTs in culture. Geochemical Perspectives Letters 19, 36–39. https://doi.org/10.7185/geochemlet.2132
Halamka, T.A., Raberg, J.H., McFarlin, J.M., Younkin, A.D., Mulligan, C., Liu, X.-L., Kopf, S.H., 2023. Production of diverse brGDGTs by Acidobacterium Solibacter usitatus in response to temperature, pH, and O2 provides a culturing perspective on brGDGT proxies and biosynthesis. Geobiology 21, 102–118. https://doi.org/10.1111/gbi.12525
Herbert, T.D., Lawrence, K.T., Tzanova, A., Peterson, L.C., Caballero-Gill, R., Kelly, C.S., 2016. Late Miocene global cooling and the rise of modern ecosystems. Nat. Geosci. 9, 843. https://doi.org/10.1038/ngeo2813https://www.nature.com/articles/ngeo2813#supplementary-information
Hess, A.V., Auderset, A., Rosenthal, Y., Miller, K.G., Zhou, X., Sigman, D.M., Martínez-García, A., 2023. A well-oxygenated eastern tropical Pacific during the warm Miocene. Nature 619, 521–525. https://doi.org/10.1038/s41586-023-06104-6
Hopmans, E.C., Weijers, J.W.H., Schefuß, E., Herfort, L., Sinninghe Damsté, J.S., Schouten, S., 2004. A novel proxy for terrestrial organic matter in sediments based on branched and isoprenoid tetraether lipids. Earth Planet. Sci. Lett. 224, 107–116. https://doi.org/10.1016/j.epsl.2004.05.012
Hoyer, S., Hamman, J., 2017. xarray: ND labeled arrays and datasets in Python. Journal of Open Research Software 5.
Huguet, C., Schimmelmann, A., Thunell, R., Lourens, L.J., Sinninghe Damsté, J.S., Schouten, S., 2007. A study of the TEX86 paleothermometer in the water column and sediments of the Santa Barbara Basin, California. Paleoceanography 22. https://doi.org/10.1029/2006pa001310
Jean-Claude, D., 1977. OSIRIS 3 - MD 13 cruise, R/V Marion Dufresne.

Jenny, J.-P., Francus, P., Normandeau, A., Lapointe, F., Perga, M.-E., Ojala, A., Schimmelmann, A., Zolitschka, B., 2016. Global spread of hypoxia in freshwater ecosystems during the last three centuries is caused by rising local human pressure. Glob. Chang. Biol. 22, 1481–1489. https://doi.org/10.1111/gcb.13193

Ji, Q., Buitenhuis, E., Suntharalingam, P., Sarmiento, J.L., Ward, B.B., 2018. Global nitrous oxide production determined by oxygen sensitivity of nitrification and denitrification. Global Biogeochem. Cycles 32, 1790–1802. https://doi.org/10.1029/2018gb005887

Lengger, S.K., Hopmans, E.C., Sinninghe Damsté, J.S., Schouten, S., 2014. Fossilization and degradation of archaeal intact polar tetraether lipids in deeply buried marine sediments (Peru Margin). Geobiology 12, 212–220. https://doi.org/10.1111/gbi.12081

Li, H., Lü, X., Tao, C., Han, T., Hu, P., Zhang, G., Yu, Z., Dong, C., Shao, Z., 2018. Distribution of tetraether lipids in sulfide chimneys at the Deyin hydrothermal field, southern Mid-Atlantic Ridge: Implication to chimney growing stage. Sci. Rep. 8, 8060. https://doi.org/10.1038/s41598-018-26166-1

Li, Z., Zhang, Y.G., Torres, M., Mills, B.J.W., 2023. Neogene burial of organic carbon in the global ocean. Nature 613, 90–95. https://doi.org/10.1038/s41586-022-05413-6

Lipp, J.S., Hinrichs, K.-U., 2009. Structural diversity and fate of intact polar lipids in marine sediments. Geochim. Cosmochim. Acta 73, 6816–6833. https://doi.org/10.1016/j.gca.2009.08.003

Liu, X., Lipp, J.S., Hinrichs, K.-U., 2011. Distribution of intact and core GDGTs in marine sediments. Org. Geochem. 42, 368–375. https://doi.org/10.1016/j.orggeochem.2011.02.003

Liu, X.-L., Summons, R.E., Hinrichs, K.-U., 2012. Extending the known range of glycerol ether lipids in the environment: structural assignments based on tandem mass spectral fragmentation patterns. Rapid Commun. Mass Spectrom. 26, 2295–2302. https://doi.org/10.1002/rcm.6355

Liu, X.-L., Zhu, C., Wakeham, S.G., Hinrichs, K.-U., 2014. In situ production of branched glycerol dialkyl glycerol tetraethers in anoxic marine water columns. Mar. Chem. 166, 1–8. https://doi.org/10.1016/j.marchem.2014.08.008

Lu, W., Rickaby, R.E.M., Hoogakker, B.A.A., Rathburn, A.E., Burkett, A.M., Dickson, A.J., Martínez-Méndez, G., Hillenbrand, C.-D., Zhou, X., Thomas, E., Lu, Z., 2020. I/Ca in epifaunal benthic foraminifera: A semi-quantitative proxy for bottom water oxygen in a multi-proxy compilation for glacial ocean deoxygenation. Earth Planet. Sci. Lett. 533, 116055. https://doi.org/10.1016/j.epsl.2019.116055

Marcantonio, F., Hostak, R., Hertzberg, J.E., Schmidt, M.W., 2020. Deep Equatorial Pacific Ocean Oxygenation and Atmospheric CO2 Over The Last Ice Age. Sci. Rep. 10, 6606. https://doi.org/10.1038/s41598-020-63628-x

Marcantonio, F., Lyle, M., Ibrahim, R., 2014. Particle sorting during sediment redistribution processes and the effect on 230Th-normalized mass accumulation rates. Geophys. Res. Lett. 41, 5547–5554. https://doi.org/10.1002/2014GL060477

Martínez-Sosa, P., Tierney, J.E., Stefanescu, I.C., Dearing Crampton-Flood, E., Shuman, B.N., Routson, C., 2021. A global Bayesian temperature calibration for lacustrine brGDGTs. Geochim. Cosmochim. Acta 305, 87–105. https://doi.org/10.1016/j.gca.2021.04.038

Peterse, F., van der Meer, J., Schouten, S., Weijers, J.W.H., Fierer, N., Jackson, R.B., Kim, J.-H., Sinninghe Damsté, J.S., 2012. Revised calibration of the MBT–CBT paleotemperature proxy based on branched tetraether membrane lipids in surface soils. Geochim.

672 Cosmochim. Acta 96, 215–229. https://doi.org/10.1016/j.gca.2012.08.011
673 Raberg, J.H., Miller, G.H., Geirsdóttir, Á., Sepúlveda, J., 2023. Near-universal trends in
674 brGDGT lipid distributions in nature. Science Advances 8, eabm7625.
675 https://doi.org/10.1126/sciadv.abm7625
676 Rathburn, A.E., Willingham, J., Ziebis, W., Burkett, A.M., Corliss, B.H., 2018. A New
677 Biological Proxy for Deep-Sea Paleo-Oxygen: Pores of Epifaunal Benthic Foraminifera.
678 Sci. Rep. https://doi.org/10.1038/s41598-018-27793-4
679 Saravanan, P., Gupta, A.K., Zheng, H., Rai, S.K., Panigrahi, M.K., 2020. Changes in Deep-Sea
680 Oxygenation in the Northeast Pacific Ocean During 32–10 ka. Geophys. Res. Lett. 47,
681 e2019GL086613. https://doi.org/10.1029/2019GL086613
682 Schouten, S., Hopmans, E.C., Schefuss, E., Sinninghe Damsté, J.S., 2002. Distributional
683 variations in marine crenarchaeotal membrane lipids: a new tool for reconstructing
684 ancient sea water temperatures? Earth Planet. Sci. Lett. 204, 265–274.
685 Shipboard Scientific Party, 1992. Site 850, in: Pisias, N.G., Janecek, T.R., Baldauf, J.G.,
686 Bloomer, S.F., Dadey, K.A., Emeis, K.-C., Farrell, J., Flores, J.A., Galimov, E.M.,
687 Hagelberg, T.K., Holler, P., Hovan, S.A., Iwai, M., Kemp, A.E.S., Kim, D.C.,
688 Klinkhammer, G., Leinen, M., Levi, S., Levitan, M.A., Lyle, M.W., MacKillop, A.K.,
689 Meynadier, L.M., Mix, A.C., Moore, T.C., Raffi, I., Ravelo, C., Schneider, D.,
690 Shackleton, N.J., Valet, J.-P., Vincent, E., Mayer, L.A., Pisias, N.G., Janecek, T.R.,
691 Baldauf, J.G., Bloomer, S.F., Dadey, K.A., Emeis, K.-C., Farrell, J., Flores, J.A.,
692 Galimov, E.M., Hagelberg, T.K., Holler, P., Hovan, S.A., Iwai, M., Kemp, A.E.S., Kim,
693 D.C., Klinkhammer, G., Leinen, M., Levi, S., Levitan, M.A., Lyle, M.W., MacKillop,
694 A.K., Meynadier, L.M., Mix, A.C., Moore, T.C., Raffi, I., Ravelo, C., Schneider, D.,
695 Shackleton, N.J., Valet, J.-P., Vincent, E., Stewart, S.K., Kennett, D., Stewart, N.J.,
696 Winkler, W.R. (Eds.), Proceedings of the Ocean Drilling Program, 138 Initial Reports,
697 Proceedings of the Ocean Drilling Program; Initial Reports; Part 1, Eastern Equatorial
698 Pacific; Covering Leg 138 of the Cruises of the Drilling Vessel JOIDES Resolution,
699 Balboa, Panama, to San Diego, California, Sites 844-854, 6 May 1991-5 July 1991.
700 Ocean Drilling Program, Ocean Drilling Program, College Station, TX, United States, p.
701 809. https://doi.org/10.2973/odp.proc.ir.138.115.1992
702 Sinninghe Damsté, J.S., Hopmans, E.C., Pancost, R.D., Schouten, S., Geenevasen, J.A.J., 2000.
703 Newly discovered non-isoprenoid glycerol dialkyl glycerol tetraether lipids in sediments.
704 Chem. Commun. 1683–1684. https://doi.org/10.1039/B004517I
705 Studer, A.S., Mekik, F., Ren, H., Hain, M.P., Oleynik, S., Martínez-García, A., Haug, G.H.,
706 Sigman, D.M., 2021. Ice Age-Holocene Similarity of Foraminifera-Bound Nitrogen
707 Isotope Ratios in the Eastern Equatorial Pacific. Paleoceanography and Paleoclimatology
708 36, e2020PA004063. https://doi.org/10.1029/2020PA004063
709 Tian, J., Fan, L., Liu, H., Liu, J., Li, Y., Qin, Q., Gong, Z., Chen, H., Sun, Z., Zou, L., Wang, X.,
710 Xu, H., Bartlett, D., Wang, M., Zhang, Y.-Z., Zhang, X.-H., Zhang, C.L., 2018. A nearly
711 uniform distributional pattern of heterotrophic bacteria in the Mariana Trench interior.
712 Deep Sea Res. Part I 142, 116–126. https://doi.org/10.1016/j.dsr.2018.10.002
713 Tierney, J.E., Russell, J.M., 2009. Distributions of branched GDGTs in a tropical lake system:
714 Implications for lacustrine application of the MBT/CBT paleoproxy. Org. Geochem. 40,
715 1032–1036. https://doi.org/10.1016/j.orggeochem.2009.04.014
716 Tribovillard, N., Algeo, T.J., Lyons, T., Riboulleau, A., 2006. Trace metals as paleoredox and
717 paleoproductivity proxies: An update. Chem. Geol. 232, 12–32.

https://doi.org/10.1016/j.chemgeo.2006.02.012
Wang, X.T., Wang, Y., Auderset, A., Sigman, D.M., Ren, H., Martínez-García, A., Haug, G.H., Su, Z., Zhang, Y.G., Rasmussen, B., Sessions, A.L., Fischer, W.W., 2022. Oceanic nutrient rise and the late Miocene inception of Pacific oxygen-deficient zones. Proceedings of the National Academy of Sciences 119, e2204986119. https://doi.org/10.1073/pnas.2204986119
Weijers, J.W.H., Schouten, S., Hopmans, E.C., Geenevasen, J.A.J., David, O.R.P., Coleman, J.M., Pancost, R.D., Sinninghe Damsté, J.S., 2006a. Membrane lipids of mesophilic anaerobic bacteria thriving in peats have typical archaeal traits. Environ. Microbiol. 8, 648–657. https://doi.org/10.1111/j.1462-2920.2005.00941.x
Weijers, J.W.H., Schouten, S., Spaargaren, O.C., Sinninghe Damsté, J.S., 2006b. Occurrence and distribution of tetraether membrane lipids in soils: Implications for the use of the TEX86 proxy and the BIT index. Org. Geochem. 37, 1680–1693. https://doi.org/10.1016/j.orggeochem.2006.07.018
Weijers, J.W.H., Schouten, S., van den Donker, J.C., Hopmans, E.C., Sinninghe Damsté, J.S., 2007. Environmental controls on bacterial tetraether membrane lipid distribution in soils. Geochim. Cosmochim. Acta 71, 703–713. https://doi.org/10.1016/j.gca.2006.10.003
Xie, S., Liu, X.-L., Schubotz, F., Wakeham, S.G., Hinrichs, K.-U., 2014. Distribution of glycerol ether lipids in the oxygen minimum zone of the Eastern Tropical North Pacific Ocean. Org. Geochem. 71, 60–71. https://doi.org/10.1016/j.orggeochem.2014.04.006
Yin, S., Hernández-Molina, F.J., Jutzeler, M., Li, J., 2022. Progressive intensification of pacific Deep Water circulation since the early Pliocene. Geophys. Res. Lett. 49. https://doi.org/10.1029/2022gl098051
Zachos, J., Pagani, M., Sloan, L., Thomas, E., Billups, K., 2001. Trends, Rhythms, and Aberrations in Global Climate 65 Ma to Present. Science 292, 686–693. https://doi.org/10.1126/science.1059412
Zell, C., Kim, J.-H., Moreira-Turcq, P., Abril, G., Hopmans, E.C., Bonnet, M.-P., Sobrinho, R.L., Damsté, J.S.S., 2013. Disentangling the origins of branched tetraether lipids and crenarchaeol in the lower Amazon River: Implications for GDGT-based proxies. Limnol. Oceanogr. 58, 343–353. https://doi.org/10.4319/lo.2013.58.1.0343
Zeng, Z., Xiao, W., Zheng, F., Chen, Y., Zhu, Y., Zhang, C., 2023. Enhanced production of highly methylated brGDGTs linked to anaerobic bacteria from sediments of the Mariana Trench. Frontiers in Marine Science 10. https://doi.org/10.3389/fmars.2023.1233560
Zhang, Y.G., Pagani, M., Liu, Z., 2014. A 12-Million-Year Temperature History of the Tropical Pacific Ocean. Science 344, 84–87. https://doi.org/10.1126/science.1246172
Zhang, Y.G., Zhang, C.L., Liu, X.-L., Li, L., Hinrichs, K.-U., Noakes, J.E., 2011. Methane Index: a tetraether archaeal lipid biomarker indicator for detecting the instability of marine gas hydrates. Earth Planet. Sci. Lett. 307, 525–534.
Zhou, X., Thomas, E., Rickaby, R.E.M., Winguth, A.M.E., Lu, Z., 2014. I/Ca evidence for upper ocean deoxygenation during the PETM. Paleoceanography 29, 964–975. https://doi.org/10.1002/2014PA002702